RESEARCH ARTICLE
SPACE PHYSICS: MAGNETOSPHERIC PHYSICS

Earth and Planetary Physics
8: 258–274, 2024
doi: 10.26464/epp2023063

Converting TREx-RGB green-channel data to 557.7 nm auroral intensity: Methodology and initial results

Jun Liang*, D. M. Gillies, E. Spanswick, and E. F. Donovan

University of Calgary, Calgary, T2N 1N4, Canada

Key Points:

- We investigate the conversion of TREx-RGB green-channel into absolute 557.7 nm intensity.
- We demonstrate the calibration procedure and empirical formula for TREX-RGB green-channel.
- We perform cross-calibration among TREx-RGB, spectrograph, and TREx-ATM model.

Citation: Liang, J., Gillies, D. M., Spanswick, E., and Donovan, E. F. (2024). Converting TREx-RGB green-channel data to 557.7 nm auroral intensity: Methodology and initial results. *Earth Planet. Phys.*, *8*(1), 258–274. http://doi.org/10.26464/epp2023063

Abstract: The recently deployed Transition Region Explorer (TREx)-RGB (red-green-blue) all-sky imager (ASI) is designed to capture "true color" images of the aurora and airglow. Because the 557.7 nm green line is usually the brightest emission line in visible auroras, the green channel of a TREx-RGB camera is usually dominated by the 557.7 nm emission. Under this rationale, the TREx mission does not include a specific 557.7 nm imager and is designed to use the RGB green-channel data as a proxy for the 557.7 nm aurora. In this study, we present an initial effort to establish the conversion ratio or formula linking the RGB green-channel data to the absolute intensity of 557.7 nm auroras, which is crucial for quantitative uses of the RGB data. We illustrate two approaches: (1) through a comparison with the collocated measurement of green-line auroras from the TREx spectrograph, and (2) through a comparison with the modeled green-line intensity according to realistic electron precipitation flux measurements from low-Earth-orbit satellites, with the aid of an auroral transport model. We demonstrate the procedures and provide initial results for the TREx-RGB ASIs at the Rabbit Lake and Lucky Lake stations. The RGB response is found to be nonlinear. Empirical conversion ratios or formulas between RGB green-channel data and the green-line auroral intensity are given and can be applied immediately by TREx-RGB data users. The methodology established in this study will also be applicable to the upcoming SMILE ASI mission, which will adopt a similar RGB camera system in its deployment.

Keywords: TREx; RGB; green-line aurora; auroral transport model

1. Introduction

Auroras are produced when energetic particles from the magnetosphere collide with the Earth's atmosphere. Different auroral emission lines at different wavelengths (colors) are characteristic of different transport processes of energetic particles and excitation processes in the atmosphere: the N_2^+ first-negative-group (1NG) containing peaks at 391.4/427.8/470.9 nm, the 557.7 nm and 630 nm oxygen (OI) emission lines, and the Hβ (486.1 nm) proton auroras, to name a few prominent auroral emission lines in the visible wavelength range. Among these lines, the 557.7 nm green line is usually the strongest emission line in terms of absolute intensity in the nightside aurora and is roughly on par with the 630 nm red-line emission in the dayside (e.g., Hu ZJ et al., 2009). The 557.7 nm line is an atomic oxygen emission from the $O(^1D_2–^1S_0)$ transition with typical peak emission heights at ~105–120 km in the nightside and ~130–140 km in the dayside (Partamies et al., 2022; Whiter et al., 2023). Although $O(^1D_2–^1S_0)$ is nominally a "forbidden" transition, its Einstein probability (~1.3 s^{-1}) is high enough to be considered a "quasi-prompt" emission for many research purposes and practical observations with exposure times >1 s. For a panchromatic system such as the THEMIS (Time History of Events and Macroscale Interactions during Substorms) all-sky imager (ASI; Mende et al., 2008), its raw data counts are mostly contributed by, and are widely deemed a proxy for, the green-line emissions (e.g., Liang J et al., 2019a; Gabrielse et al., 2021). Furthermore, the 557.7 nm emission intensity has often served a central role in many existing attempts to derive electron precipitation parameters from optical aurora data (e.g., Rees and Luckey, 1974; Janhunen, 2001; Hecht et al., 2006; Liang J et al., 2011; Gabrielse et al., 2021). It is fair to state that the green line represents the most often seen and the most used emission line in the visible wavelength range in auroral studies.

Ground optical observations are powerful tools used to trace the spatiotemporal variations of auroras and to remote-sense the magnetospheric dynamics driving the aurora. The Transition Region Explorer (TREx) mission currently deployed by the University of Calgary, Canada, is designed to use ground multi-instrument observations to study the energization and transport of particles and associated plasma processes in the nightside transition

Correspondence to: J. Liang, liangj@ucalgary.ca
Received 20 APR 2023; Accepted 08 SEP 2023.
First Published online 27 NOV 2023.

region, which maps to where a topological transition from a dipolar-like to a stretched magnetic field configuration transpires in the magnetotail. One key scientific objective of the TREx is to provide a two-dimensional (2-D) ionospheric projection of time-varying electron precipitation parameters (fluxes and energies) by using combined data from multi-wavelength optical instruments and imaging riometers, with the aid of an auroral transport model (ATM). The current deployment of TREx imagers includes the blue line (427.8 nm), the near-infrared (844.6 nm), the red line (630 nm) inherited from the previous Red-line Emission Geospace Observatory (REGO) mission (Liang J et al., 2016), and the RGB (red-green-blue) True Color Imager (Gillies et al., 2020). The TREx-RGB ASI is designed to capture "true color" images of the aurora and airglow. The RGB "images" are composed of three images, one through each of the three color channels: red (R), green (G), and blue (B). Because the 557.7 nm green line is usually the brightest emission line in nightside visible auroras, the green channel of a TREx-RGB camera is usually dominated by the 557.7 nm emission. Under this rationale, the TREx mission does not include a specific 557.7 nm imager and is intended to use the RGB green-channel data as a proxy for the 557.7 nm aurora. It is conceivable that the RGB data can be effectively used in tracing the locations and morphological variations of auroral structures as well as analyzing the relative changes in auroral intensities with time, as per our previous experience with Rainbow (also an RGB camera; e.g., Jackel et al., 2014; Liang J et al., 2016). The RGB camera will almost certainly perform better than the white-light ASI for the aforementioned qualitative tasks. For more quantitative studies, an appropriate conversion from the RGB green-channel data to the absolute 557.7 nm auroral intensity is highly desirable. This is also of crucial importance for our efforts to invert electron precipitation parameters from TREx datasets, the major scientific goal of the TREx mission.

This study is motivated by a few considerations:
(1) We take the initial and important step of examining whether the RGB green-channel data can be used to quantitatively infer the absolute 557.7 nm auroral intensity within a reasonable error margin.
(2) TREx data have been accumulating for several years. To the authors' knowledge, research colleagues at various institutes have already begun to use TREx-RGB data for a variety of research purposes. A pressing demand exists for a reasonable conversion of RGB data into realistic auroral intensities.
(3) Looking forward, the upcoming Solar wind Magnetosphere Ionosphere Link Explorer (SMILE) ASI, which is a complement to the SMILE (Branduardi-Raymont et al., 2018) mission and will replace the existing (and aging) THEMIS ASI network in the next 1–2 years, is designed to adopt RGB cameras similar to the TREx-RGB ASI.

The methodology and procedures established in this study will also be useful for the upcoming SMILE ASI mission. The TREx is still under deployment to date, and the calibration process is still ongoing. For example, the flat-field correction of the TREx-RGB ASI has not yet been fully implemented. As an initial study, the research goal of this paper is to evaluate the overall conversion factors over a broad field of view (FoV) and within the common range of auroral intensities. These conversion factors or formulas can be used immediately by the community for quantitative analyses of TREx-RGB data within an acceptable error margin. Subtleties such as the elevation dependence of conversion ratios across the camera will be left to future studies.

This article is organized as follows. In Section 2 we introduce the optical instruments used in this study, the TREx-RGB ASI and the spectrograph, and demonstrate the procedures used to obtain the dark/background frame for subtraction from TREx-RGB ASI measurements. In Section 3, we demonstrate the methods and procedures used to establish the empirical ratio or formula converting the RGB green-channel raw digital number to the absolute intensity of 557.7 nm auroras. Section 4 discusses certain limitations of the current study and some future works to improve the calibration, as well as some perspectives on the upcoming SMILE ASI mission. Section 5 summarizes and concludes this study.

2. Instruments

2.1 The TREx-RGB ASI and Spectrograph

Images used in this study are from the newly deployed TREx True Color Imagers (called "RGB"). The RGB (red-green-blue) ASI is a highly sensitive full-color imager designed to capture "true color" images of the aurora and airglow (Gillies et al., 2020). The RGB ASIs were developed in coordination with Canon Canada Inc. to leverage the Canon ME20F-SH high-sensitivity detector. The ME20 contains a full-frame 35 mm complementary metal oxide semiconductor (CMOS) sensor similar to a digital SLR (single-lens reflex) camera but tuned for extreme low-light performance. For the TREx-RGB, the detector is combined with a fish-eye lens and operated at a 3 Hz exposure rate; sequences of 9 frames are summed to produce 3-s data with an effective 100% duty cycle. Such a 3-s cadence dataset is used in this study. The TREx 3-s data are open to public access, whereas the 3 Hz raw RGB data is provided on request.

Figure 1a shows the color response of the ME20F-SH copied from the Canon White Paper "Advances in CMOS Image Sensors and Associated Processing." The TREx-RGB further utilizes the built-in infrared filter of the ME20 to reduce the long-wavelength response of the system. This is done to preserve the color balance and produce images with a color response similar to the human eye. Figures 1b–1d demonstrate the images from the three color channels taken from the Rabbit Lake (RABB) RGB ASI at 07:35 universal time (UT) on February 5, 2022, and Figure 1e displays the true-color composite image combining the three channels and projected into the Altitude-Adjusted Corrected Geomagnetic (AACGM) coordinates (Baker and Wing, 1989) with an emission height of 110 km. It is not surprising that auroras in the composite image appear greenish because of the dominance of the 557.7 nm green emissions. The TREx-RGB consists of a network of six cameras installed across central and northern Canada. In this study, we use data from the RGB ASIs at RABB (58.23°N, 103.68°W) and Lucky Lake (LUCK, 51.15°N, 107.26°W), both in Saskatchewan, Canada.

The TREx spectrograph (TRSp) is a high-sensitivity imaging spectrograph designed to capture emissions between ~390 and

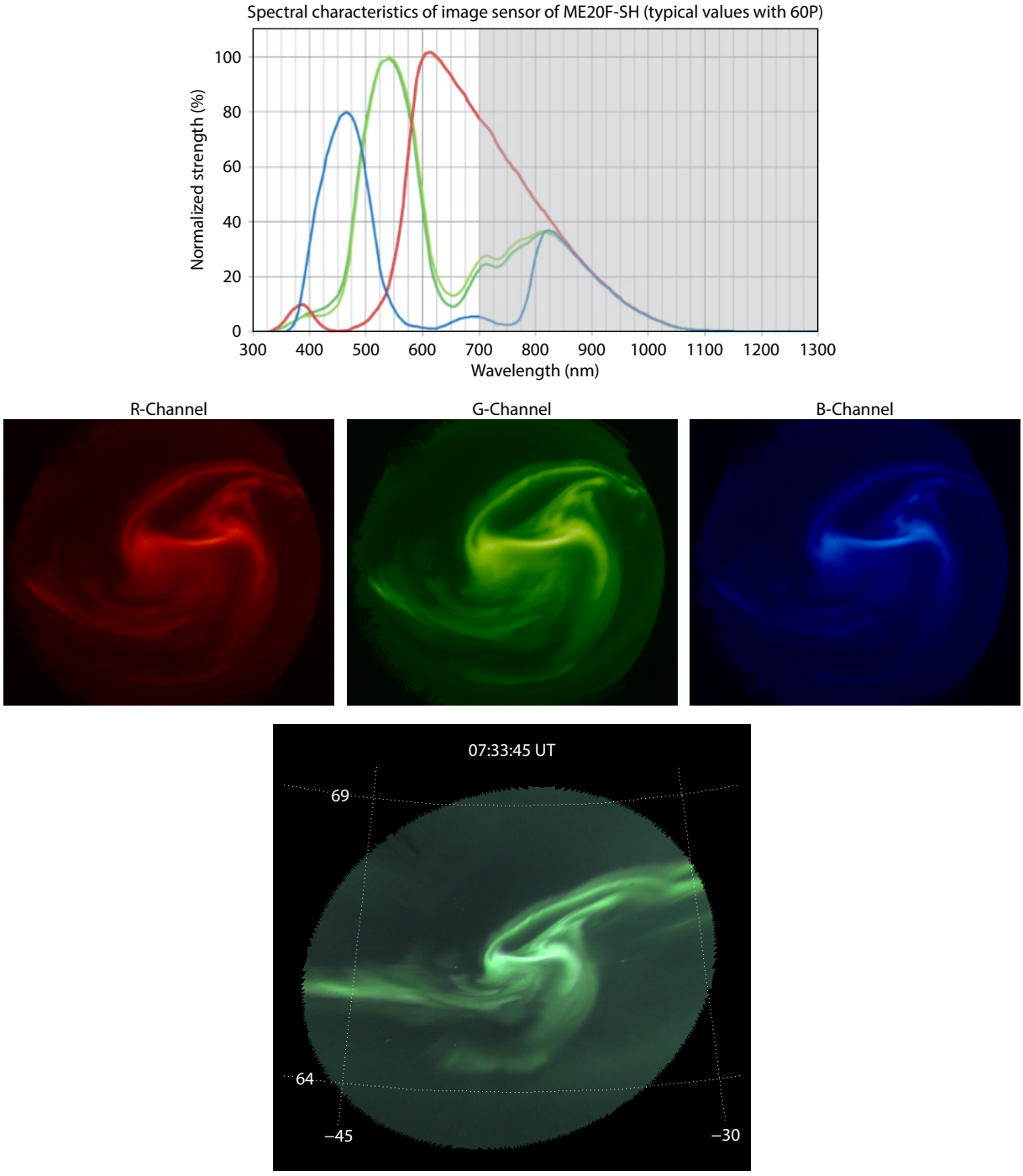

Figure 1. The top panel shows the spectral responsivity of the TREx-RGB CMOS Sensor copied from the Canon White Paper. Curves with different colors denote the filter profile for different channels. The two slightly separated green curves denote measurements using two different light sources. The long wavelength portion (>700 nm, grayed part) is suppressed by the built-in infrared cut filter. The middle three subfigures show examples of the red-, green-, and blue-channel image data taken by the RABB RGB ASI on February 5, 2022, at 07:35:45 UT. The RGB composite true-color image from the three channels above is shown in the bottom panel, which is projected to AACGM coordinates by assuming a 110 km emission height.

800 nm from nighttime aeronomic phenomena, such as airglow and auroras, across a slice of the full night sky. The TRSp operates at a 15-s cadence with a 13-s exposure time and has ~200 elevation bins (each of ~0.9° width) along a meridional line from the northern to southern horizon. Note that in all subsequent references to "elevation angle" in the text and figures, the elevation angle is counted from the northern horizon, and is 180° at the southern horizon. Raw images are processed by subtracting bias and dark signals and applying a flat-field correction (courtesy of D. Hampton at the University of Alaska Fairbanks). They are then converted to optical Rayleigh by using an absolute conversion obtained by calibrated broadband low-light-level ^{14}C phosphor sources in

conjunction with a National Institute of Standards and Technology (NIST)-traceable tungsten lamp**.** Both light sources are needed to calibrate the full wavelength range of the TRSp. For the wavelength range of interest in this study, the NIST calibration factors are applied. For further details on the TRSp instrument and calibration, see Gillies et al. (2019, 2023).

Figure 2a shows the scan line of the TRSp at RABB overplotted on an RGB ASI image taken at 07:12:15 UT on February 27, 2022. We sample the optical spectrum of an auroral arc (the sampled TRSp bin is marked as a blue circle) from the TRSp measurements, as shown in Figure 2b. It is not surprising that the 557.7 nm green-line emission constitutes the dominant peak of the auroral spectrum, whereas other major emission lines or bands, such as N_2^+ 1NG (391.4/427.8/470.9 nm), OI 630 nm red line, and N_2 First Positive Group (1PG), are also recognizable. By integrating the TRSp spectral bins over the green-line peak (in practice ±1.5 nm surrounding the maximum), we obtain the total green-line emission intensity in Rayleigh. In data processing, we also subtract a baseline, presumably consisting of ambient white light and remnant dark currents, determined from the nearby nonauroral wavelengths. The 557.7 nm auroral intensity derived from the TRSp is later used to calibrate the collocated RGB green-channel data.

2.2 The dark/background Frame of the TREx-RGB ASI

The raw green-channel digital number (GCDN) recorded by an RGB ASI may consist of the following contributing sources (e.g., Watanabe et al., 2017):

$$\mathrm{GCDN} = A_{\mathrm{grn}} + A_{\mathrm{oth}} + \mathrm{BKG} + \mathrm{DC} + \mathrm{DR}, \quad (1)$$

in which A_{grn} indicates the green-line emission of interest and A_{oth} denotes the contribution from other auroral emissions that are contained in the spectral coverage of the green channel. Using the RGB bandpass filter profile and TRSp measurements collected over 13 h on 6 nights at RABB in this study (see Section 3.1), we evaluate the mean $A_{\mathrm{oth}}/A_{\mathrm{grn}}$ ratio as being 11.5 ± 2.7%. Furthermore, A_{oth} is found to be highly correlated with A_{grn}, with a Pearson linear correlation coefficient of ~0.93, because they are both scaled by the total electron precipitation flux. The part of A_{oth} that is proportional to A_{grn} will be absorbed by our procedure and contained in the conversion factor between the GCDN and the 557.7 nm intensity. The remnant portion of A_{oth} that is uncorrelated with A_{grn} is presumably no more than a few percent of A_{grn} and is thus ignored in this study. The background (BKG) denotes the contribution from the ambient lights, such as celestial sources and nightglows. All the aforementioned light contributions inherently contain statistical counting errors, so-called "photon shot noise," which cannot be removed and are considered an intrinsic part of the data uncertainty. The abbreviation DC denotes the contribution of dark currents. In some nomenclatures, a distinction may be made between the "bias signal" and the "dark signal," contingent on the dependency on varying exposure times, but such a distinction is not necessary for our data (fixed exposure time) and the following procedure. Dark currents depict a bias offset of the digital number collected by an imager pixel even without external lights, which is temperature dependent but otherwise presumably fairly stable over a long period. The abbreviation DR denotes the dark random noise (such as readout noise), which refers to random variations independent of each exposure. As mentioned, the 3-s data used in this study come from the integration of nine 3 Hz exposure frames. In such an integration, the random noise is presumably reduced (but not eliminated). For a charge-coupled device (CCD) sensor, which has better dark current uniformity, pixels at the camera corner that are shielded from external lights may be used to evaluate the dark current. However, for a CMOS sensor the charge-to-voltage conversion is separate for each pixel so that the electronic gain, readout noise, and dark current differ from pixel to pixel (e.g., Watanabe et al., 2017). These dark currents need to be properly subtracted from the raw RGB data. Astronomical observers are familiar with the technique of obtaining a dark frame by taking shots with the aperture covered before actual observations. However, the TREx-RGB is currently scheduled to run with a full-duty cycle without dark frame acquisition. We must resort to other approximate approaches to obtain the dark/background frame. Note that we have used the term "dark/background" frame because the procedure we follow cannot actually distinguish contributions from dark currents and background lights, although the former is presumably much larger during the clear, moonlit-free night intervals that are purposefully chosen for the research goal of this study.

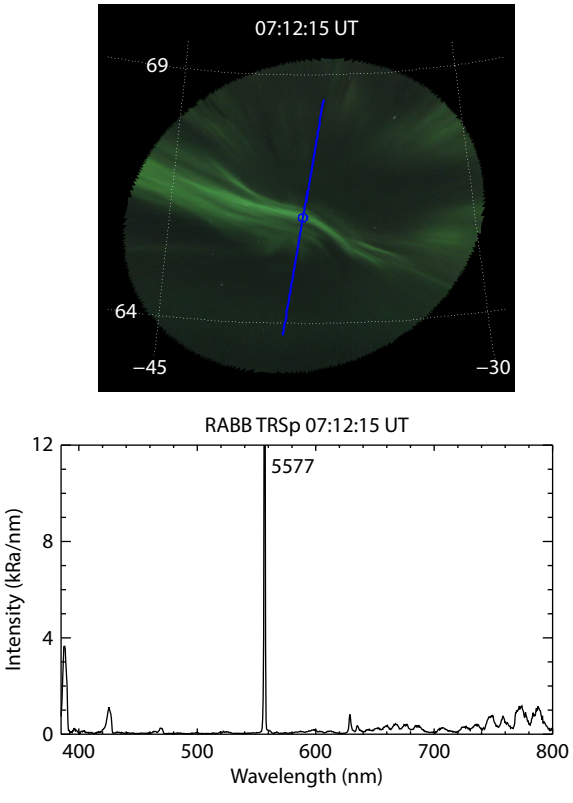

Figure 2. The upper panel shows an example RGB composite image taken on February 27, 2022, at 07:12:15 UT. The blue line indicates the TRSp scan line; the open circle indicates the TRSp bin where the auroral spectrum was sampled, as shown in the bottom panel.

Stations such as RABB are at auroral latitudes. To properly evaluate the dark/background GCDN, we need to identify quiescent intervals of auroral activities. To achieve this, we first browse the RGB ASI movie over the event night to search for quiescent times. The

selected interval must be quiescent overall for more than 1 h. Sporadic weak aurora structures might occasionally exist in the interval, but they may not affect our analysis because (1) as to be subsequently illustrated, we shall select the 10 "quietest" minutes from the >1 h quiescent interval, and the selection is done separately for individual pixels; and (2) the existence of sporadic auroras can readily be separated out by our histogram approach. We also check the geomagnetic indexes, such as *Kp*/*AE*, to help corroborate the selected quiescent intervals. Below, we shall use an event example to demonstrate the procedures we use to obtain the dark/background frame. The time interval of interest here is February 27, 2022, 06:00–08:00 UT, during which time we collect RABB RGB and TRSp data for comparison. Figure 3a shows an example of the RABB ASI green-channel image at 07:00 UT. For each pixel of the RGB ASI (we mark a red square to exemplify this in Figure 3a), we calculate the minute-averaged GCDN of this pixel, as shown in Figure 3b. The *AE* index is also overplotted for reference. The interval 03:00–05:00 UT is found to be fairly quiet, with the minimal GCDN and *AE*. We identify the 10 lowest minute-averaged GCDN (marked as dotted lines in Figure 3b) between 03:00 and 05:00 UT, and thus determine the 10 quietest minutes for the pixel of interest. We then use the 200 3-s GCDN values of the pixel from these 10 quietest minutes to construct a histogram, as shown in Figure 3c. The histogram displays a well-defined isolated peak with narrow spreads toward both sides, and no occurrence exists further toward the lower GCDN end. The aforementioned distribution is consistent with the notion of a fixed-bias dark current superimposed by random noise fluctuations. We use the mean of the peak distribution weighted by the occurrence as the dark/background value of the pixel. We run the procedures above separately for all pixels of the RGB ASI; the quietest minutes chosen and the dark/background values vary for different pixels. Finally, we use all pixels to construct the dark/background frame, as shown in Figure 3d.

We construct the dark/background frames following the procedures above for all our subsequent events (a total of 13 h on 6 nights). In most of the events, we are able to find quiescent intervals no more than ~3 h away from the UT hours of interest, either before or after. An exception comes from the SpaceX storm intervals (February 3–4, 2022), during which time long-lasting auroral intensifications persisted in the RABB FoV. For these 2 nights, we use the early periods before the storm commenced at 04:00 UT to construct the dark/background frame for February 3, 2022. The auroras were active all night during February 4, 2022, and we adopt the same dark/background frame as that constructed for February 3, 2022.

The dark/background frame we obtained is not without errors. First, the dark/background values are evaluated at different hours or even one day away (for the February 4, 2022, event) from the event time epoch of interest; the instrument temperature and the ambient light condition might somehow have changed over the time gap. Second, even though we have purposefully chosen quiescent intervals, we still cannot exclude the possible existence

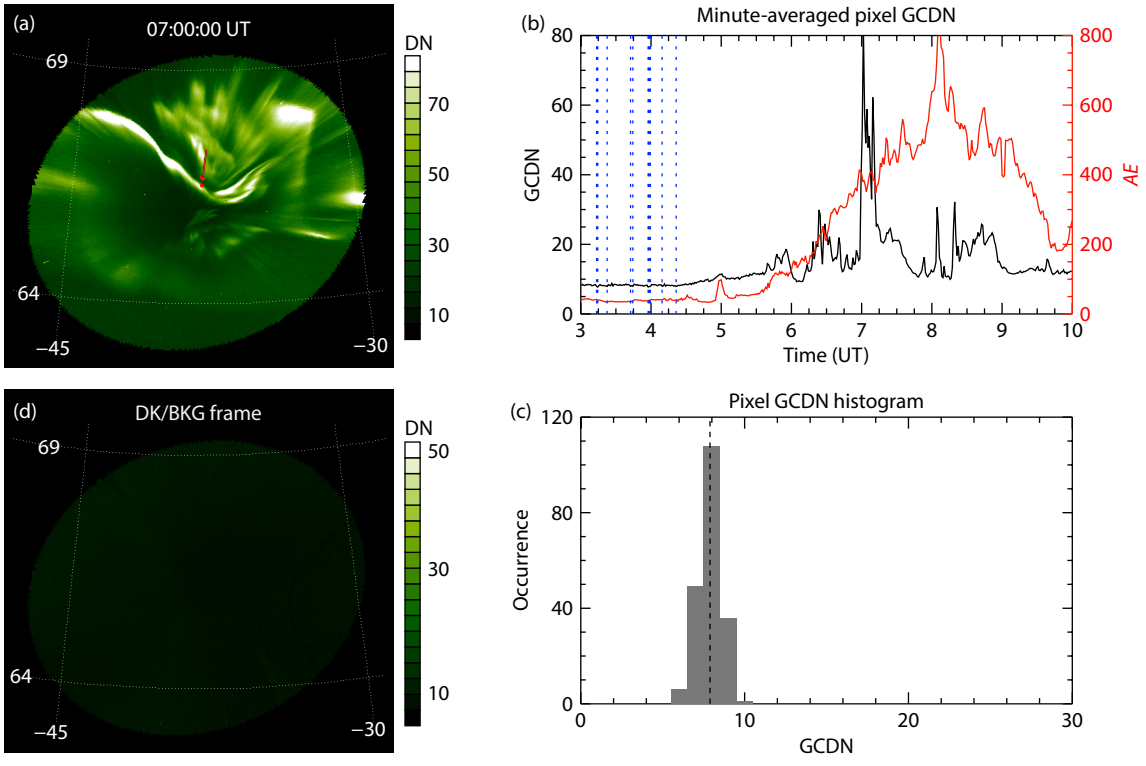

Figure 3. (a) An example of an RGB green-channel image taken on February 27, 2022, at 07:00 UT. The red arrow and square indicate the ASI bin that was used to demonstrate the procedures for obtaining the dark/background value. (b) Time variations of the minute-averaged GCDN of the selected ASI bin; the vertical dashed lines indicate the 10 quietest minutes identified. (c) A GCDN histogram of the selected bin in the 10 quietest minutes. The dashed line marks the mean of the peak distribution, which becomes the inferred dark/background value of the selected bin. (d) The dark/background frame constructed with all pixels undergoing the procedures mentioned.

of the remnant of some weak yet persistent auroras (such as ambient diffuse auroras) in the dark/background frame. We also note that uncertainty attributable to photon shot noises can be significant at very weak auroral intensities for both the RGB and TRSp. To partly relieve the uncertainties mentioned, in the following data selection and collection, data points with a GCDN below 2 times the dark/background value of the data bin are excluded. This process basically rules out the presence of weak auroral intensities. Only ~0.3% of our collected data points are found with a TRSp 557.7 nm intensity of <1.5 kRa (kiloRayleigh). Many of these rare outliers appear as isolated "spikes" when compared with data from adjacent spatial–time bins and are suspected to be led by occasional problematic or noisy data. We exclude those rare outliers by applying a 1.5 kRa threshold of the TRSp 557.7 nm intensity in the data collection. The present study may thus not be applicable to weak auroras, such as the ambient diffuse aurora. More robust ways of obtaining the dark frame (i.e., regularly taking dark frame shots with an external shutter) are under consideration for the future operation of the TREx-RGB ASI.

2.3 Preliminary Evaluation of the Flat-Field Variability

One other issue is the flat-field calibration, which corrects the pixel response across the camera FoV to a uniform input. Rigorous flat-field calibration of the TREx-RGB camera requires laboratory measurements with a standard uniform light source, which is still ongoing for the time being. As we mention later in the data analysis, we notice evidence that the conversion ratio between the GCDN and the 557.7 nm intensity seems to show moderate elevation-angle dependence, alluding to the likely existence of different pixel gains at different elevation angles. One approximate way to roughly assess the flat-field gain variability is to use statistics over a large number of auroral events that populate the camera FoV. For such a purpose, we examine cloudless moonlit-free night hours from January to March 2022 and select active auroral intervals that populate the elevation angle range of interest (30°–150°) of the RABB RGB ASI by visually browsing the keograms. Overall, a total of 28,800 RABB RGB auroral images are assembled. Figure 4a shows the GCDN image map (30°–150° elevation) averaged over all collected auroral images. We have done the dark/background subtraction for each event by using the aforementioned procedures and have applied the threshold that the GCDN must be >2 times the dark/background value for a pixel to be involved in the averaging. Figure 4b shows the mean and standard deviation of the GCDN at each elevation angle bin along the TRSp scan line. The overall averaged GCDN of all assembled data points is shown by a horizontal dashed line. The mean GCDN features a relatively flat minimum (~18.6–18.8) surrounding the zenith, yet it increases to ~22.7 at 30°–150° elevation angles. The higher apparent GCDN at oblique elevation angles is partly due to the line-of-sight (LOS) integral effect along slant paths. Note that such an LOS integral effect will also affect the TRSp measurements and thus has little influence on the evaluation of the conversion ratio between the GCDN and TRSp 557.7 nm intensity. Other factors contributing to the flat-field variability include pixel sensitivity and distortion in the optical path. In any case, we notice that the variation in the mean GCDN across elevation angles is no more than ±14% with respect to the overall averaged GCDN (~20). As the research goal

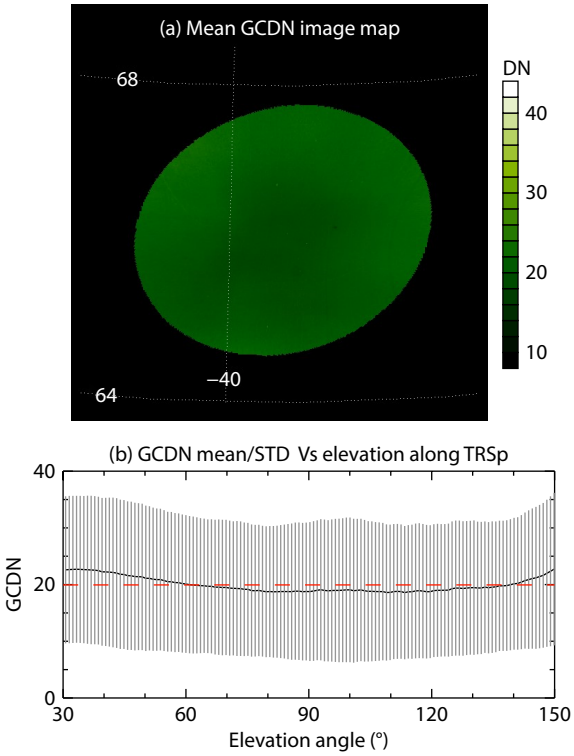

Figure 4. (a) The dark/background subtracted GCDN image map (30°–150° elevation) averaged over 28,800 auroral images. (b) Mean (circles) and standard deviation (vertical bars) of the GCDN at each elevation angle bin along the TRSp scan line. The overall averaged GCDN of all data points is shown by the red dashed line.

of this initial study, we intend to establish the overall conversion factor averaged over elevation angles of 30°–150° and within the common range of auroral intensities. The result above may then be used to roughly assess the error of such overall conversion factors led by the flat-field variability across the elevation angles of interest. Considering the presence of other error sources, we expect an error margin of approximately ±20% of our derived conversion factors, which would be deemed acceptable for the purpose of this initial study. A more delicate study considering the subtle variations in conversion factors across the ASI FoV will be left as a future task contingent on the accomplishment of the laboratory flat-field correction.

3. Calibration with the TRSp and TREx-ATM

3.1 RABB RGB Calibration with the TRSp

In this subsection, we use the TRSp-inferred 557.7 nm intensity to calibrate the RGB GCDN at RABB. We first use the February 3, 2022, 11:00–12:00 UT interval to exemplify our procedures, as well as the definitions and criteria involved. One reason we choose this event for demonstration is that in the next subsection, we use the same event interval to exemplify the TREx-ATM-based calibration approach. The same dark/background frame is applied in both approaches so that it will not constitute an error source for the difference of the results in the two approaches. Figure 5a shows the keogram of the 557.7 nm intensities versus time and elevation angles obtained from the TRSp measurements during the interval of interest. To sample the RGB ASI GCDN data for comparison, we

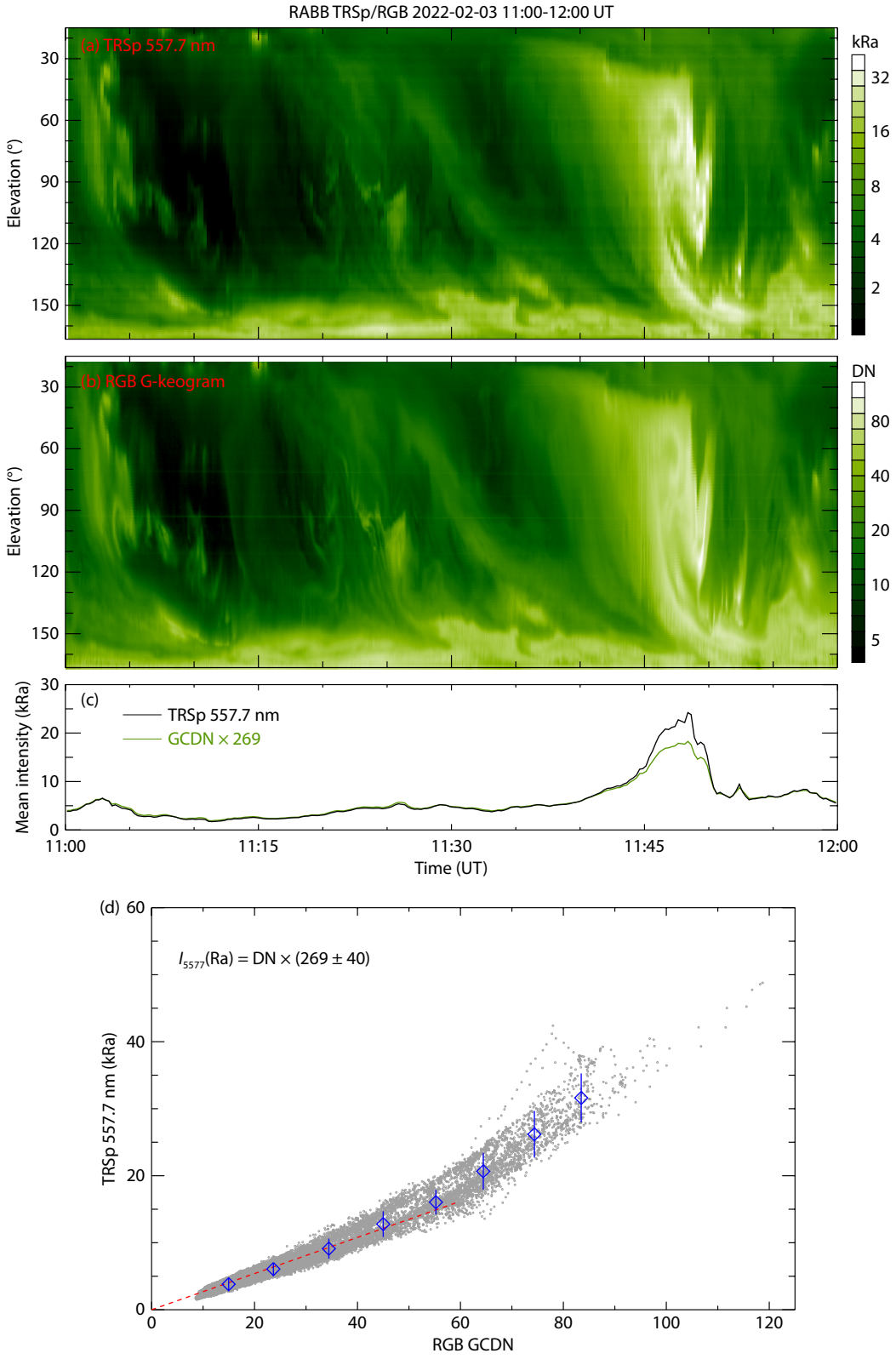

Figure 5. (a) Keogram of the 557.7 nm intensity obtained from the TRSp versus time and elevation angle on February 3, 2022, from 11:00 to 12:00 UT. The elevation is 0°/180° at the northern/southern horizon. (b) Keogram constructed from dark/background subtracted RGB GCDN sampled along the TRSp scan line. (c) Mean intensity integrated over the 30°–150° elevation range for the TRSp at 557.7 nm (black) and for the RGB GCDN along the TRSp scan line (green, multiplied by 269). (d) Scatterplot of the collected data points of the GCDN and the TRSp 557.7 nm intensity on February 3, 2022, from 11:00 to 12:00 UT. The red dashed line marks the best linear fit at a GCDN of <60. The blue diamonds and lines indicate the mean and standard deviation of 557.7 nm intensities in successive GCDN bins beginning at 10, with each having a width of 10.

first construct the dark/background frame for the UT hour by using the procedures depicted in Section 2.2. Figure 5b shows the keogram of the dark/background-subtracted GCDN sampled along the TRSp scan line during the event interval. This step is done by sampling and averaging within ±0.15° magnetic longitude (mlon) around the TRSp scan line at each latitude. A high degree of conformity between the time–elevation distribution of the auroral intensities on the two instruments is straightforward to see, except that some subtle differences exist at the lowest edge of the FoV. We have constructed and browsed these keograms for all 13 h of event intervals to be investigated hereafter. Occasionally, suspicious glitch epochs and data points noticeable on the keograms are carefully checked and removed.

It is well known that all optical instruments are subject to more errors and uncertainties at low elevation angles. Although it is true that the TRSp and RGB ASI are collocated so that some errors led by low elevation angles are shared, they are still separate instruments with different optical designs. Some of the error sources, such as pixel displacement, sky map inaccuracy (e.g., Gillies et al., 2017), and stray light contamination (e.g., Peterson, 1999), are specific to individual instruments. Furthermore, recall that the flat-field correction, which may have the largest influence at low elevation angles, is not yet complete for the RGB. Taking into account the considerations above, in this study we limit our interest to the 30°–150° elevation angles in collecting TRSp-RGB data for comparison. Within such an elevation angle range, sky map inaccuracy usually does not result in significant displacement of auroral structures with horizontal scales >10 km, and the flat-field variability might not be severe, as per our preliminary evaluation presented in Section 2.3. Figure 5c shows the mean intensity of the TRSp 557.7 nm (black curve) averaged over the 30°–150° elevation range and that of the RGB GCDN along the TRSp line (green curve). The latter is multiplied by a factor of 269, a best-fit linear conversion ratio to be elucidated in the following analysis. As one can see, the two curves largely overlap, with a correlation as high as 0.99. This observation corroborates that the TREx-RGB green channel can be used as a proxy for the 557.7 nm auroral emission. Noticeable differences up to ~30% between the two curves in Figure 5c exist only when the mean 557.7 nm intensity is above ~20 kRa; the ratio between the GCDN and the green-line intensity there is larger than 269, for the reason we shall elucidate in the following paragraph.

We sample the GCDN values along the TRSp scan line over the elevation angle range of 30°–150° and integrate or organize them into the same spatial and time bins (~0.9° elevation bin and 15-s cadence) of the TRSp. Figure 5d shows the scatterplot of the sampled GCDN versus the concurrent, collocated TRSp green-line intensities. As one can see, the GCDN and the 557.7 nm intensity (I_{5577}) are overall positively correlated. Notwithstanding certain scatter (to be addressed in the following paragraph), the overall response appears to be close to linear up to a GCDN of ~60. We calculate the linear coefficient C by assuming $I_{5577} = C \cdot \mathrm{GCDN}$ and performing a least-squares fit to the data with GCDN values of <60; the best-fit line and the obtained linear ratio (269) are marked in the plot. The 1-σ uncertainty (±40) of such a ratio is technically defined as the range surrounding the best-fit ratio that contains 68.3% of the total data points with GCDN values of <60. The procedures and definition above are used throughout this study. To facilitate readers' ability to discern the general trend of the response and its transition from quasi-linear to nonlinear, we group the data into GCDN bins with a width of 10 (10–20, 20–30, 30–40, etc.) and calculate the mean 557.7 nm intensity and the standard deviation of the data points in each bin. The mean and standard deviation in each bin are overplotted in Figure 5d. Our quantitative criterion to judge where a quasi-linear trend still holds is that the mean 557.7 nm intensity in a certain GCDN bin is within the 1-σ range of the linear slope fitted from all previous GCDN bins. Using this criterion, we find that the quasi-linear trend holds up to the [50, 60] GCDN bin. The mean 557.7 nm intensity and the 1-σ range in GCDN bins of >60 are distinctly higher than the linear slope fitted in GCDN $\in$ [10, 60], so we can infer that the response deviates from the previous linear trend at GCDN values of >60.

Upon closer examination of the data, we find that one main reason contributing to the scatter of data points in Figure 5d, other than data noise and sky map inaccuracy, is that the data points collected at different elevation angles tend to have different ratios between the GCDN and the 557.7 nm intensity. This result is very likely related to the variations in pixel gains across the FoV. Although a rigorous flat-field calibration of the TREx-RGB is not yet fully complete, we have presented in Section 2.3 a rough assessment of the flat-field variability by using a large number of auroral images. We note that our derived 1-σ uncertainty (~14.9%) of the linear ratio is compatible with the estimated flat-field variability shown in Section 2.3. We emphasize again that the intent of this work is to provide an approximate evaluation of the conversion factor between the GCDN and 557.7 nm intensities over a broad range of the ASI FoV. A more accurate determination of the angular dependence of conversion factors will be performed once the flat-field calibration of the RGB ASI is completed.

We have searched through TREx datasets to select time intervals suitable for a comparative study between the RABB RGB ASI and TRSp. Our criteria were as follows:
(1) Both instruments operated normally with no marked anomalies in the system monitoring records.
(2) The sky condition was clear, without moonlit or other noticeable light contamination.
(3) Strong auroral activities were within the elevation angle range of interest, reaching above ~30 kRa as our threshold. This threshold was imposed to ensure that the data spread could embody a transition from quasi-linear to nonlinear RGB responses, to be elucidated later in this subsection.

To date, we have selected and collected 13 h of data from 6 nights: (1) February 3, 2022, at 06:00–07:00 UT; (2) February 3, 2022, at 09:00–10:00 UT; (3) February 3, 2022, at 11:00–12:00 UT; (4) February 4, 2022, at 03:00–04:00 UT; (5) February 4, 2022, at 05:00–06:00 UT; (6) February 4, 2022, at 08:00–09:00 UT; (7) February 4, 2022, at 09:00–10:00 UT; (8) February 5, 2022, at 07:00–08:00 UT; (9) February 24, 2022, at 02:00–03:00 UT; (10) February 24, 2022, at 06:00–07:00 UT; (11) February 27, 2022, at 06:00–07:00 UT; (12) February 27, 2022, at 07:00–08:00 UT; (13) March 4, 2022, at 06:00–07:00 UT. The selected time intervals involve various

major auroral types, such as poleward boundary intensifications, substorm intensifications, and pulsating auroras, among others. We also note that the local magnetic midnight occurs at ~07:30 UT at RABB, so the selected time intervals cover an even distribution in the premidnight, midnight, and postmidnight sectors.

We assemble all data points collected from the aforementioned events, as shown in Figure 6a. Overall, ~250,000 data points are involved. Because too many data points are clustered, we also present in Figure 6b their density distribution. Each bin in Figure 6b represents the percentage of data points contained in such a bin. Also note that Figure 6b is plotted with log-scale axes. Potential causes of the scatter of data points include photon shot noise, sky map inaccuracy, fine-scale temporal oscillations of auroras (see the specific discussion later in this subsection), and the sensor gain variations over elevation angles mentioned previously. Nevertheless, considering the fact that the data are collected over 13 different hours on 6 nights, the scatter is satisfactorily limited, and the overall trend is well defined. Following the procedure depicted above, in Figure 5d we overplot the mean and standard deviation of the 557.7 nm intensities in successive GCDN bins, each with a width of 10. Using the aforementioned criteria, we note again that the response is quasi-linear for GCDN values up to ~60 and that the best-fit linear ratio is calculated as ~277 ± 43 for

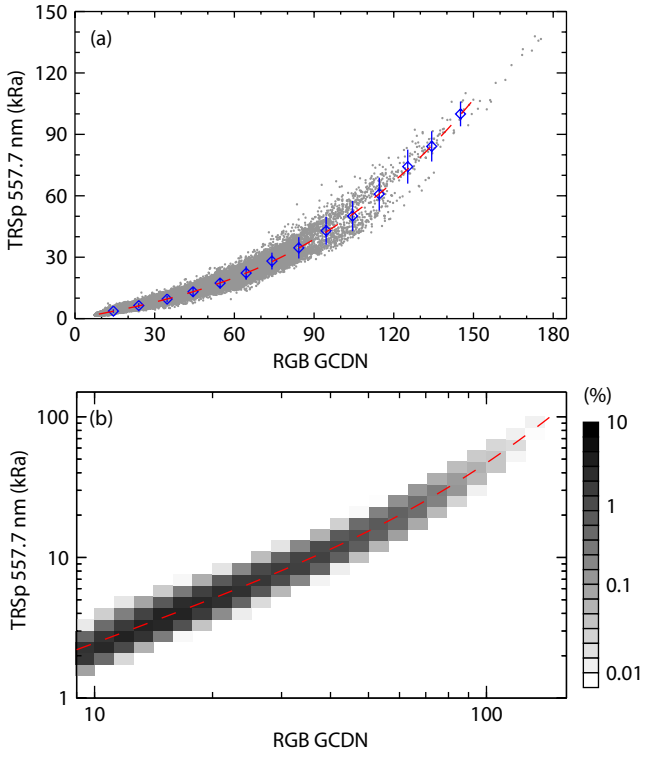

Figure 6. (a) Scatterplot of collected data points of the GCDN and the TRSp 557.7 nm intensity at all intervals. The blue diamonds and lines indicate the mean and standard deviation of 557.7 nm intensities in successive GCDN bins beginning at 10, with each having a width of 10. (b) The density distribution corresponding to the scatterplot (a). In both (a) and (b), the red dashed curve denotes the empirical fit according to Equation (2).

GCDN values of <60. At higher GCDN values or, equivalently, when the 557.7 nm intensity is ≥~20 kRa, the response becomes obviously nonlinear. To obtain an empirical formula linking the GCDN and the 557.7 nm intensity, we make the following fit to the dataset in the range of GCDN ∈ [9, 150]:

$$I_{5577}\,(\mathrm{Ra}) = a_1 \cdot \mathrm{GCDN} \cdot \left(1 + a_2 \cdot \mathrm{GCDN}^{a_3}\right), \tag{2}$$

$$a_1 = 242.486,\ a_2 = 2.394 \times 10^{-4},\ a_3 = 1.796.$$

The main reason for the nonlinear response at high auroral intensities is presumably due to the saturation of the CMOS sensor. All photon-electronic optical instruments are subject to saturation or blooming when the light input exceeds a certain threshold. Even though the CMOS technology has advanced substantially in recent decades, its dynamic range and linearity are still often under par as compared with the high-end scientific CCD. To fully quantify the nonlinearity of the CMOS sensor, laboratory measurements using standard light sources with varying exposure times are required, which will be done in the near future. Such inherent nonlinearity of the RGB response incurs a complication that may lead to concerns about our procedure and results, under the circumstance of rapidly varying auroras with timescales much shorter than the time resolution of the TRSp (~15 s). This result may be due to either temporal fluctuations or spatial aliasing led by fast-moving small-scale auroras sweeping over the TRSp scan line. Strong auroras are typically dynamic. In our comparative analysis, we integrate the RGB measurements to have the same integration time as the TRSp. The nonlinear response of the RGB would make the integrated RGB response contingent on the fine-scale time-varying characteristics of the auroras. in the following paragraph, we perform a semiquantitative check of the potential influence of varying auroras within the TRSp integration time. We compare two derived quantities for each data point: One uses the mean GCDN integrated over the TRSp integration time, as we did in the procedures above, and Equation (2) to model the 557.7 nm intensity (labeled as I_0). The other uses the individual 3-s frame GCDN and Equation (2) to model the 557.7 nm intensity in each 3-s frame, and then the average over the TRSp integration time (labeled as I_1). As shown in the Supplementary Materials, when other error sources are ignored, the difference between I_0 and I_1 can be used to approximately evaluate the error of the empirical fit led by time-varying auroras. If the RGB response is linear, if the auroras are steady, or both, there would be no difference between I_0 and I_1. In the presence of nonlinearity, if I_0 and I_1 have a large systematic difference, the fluctuating auroral intensities within the TRSp integration time are inferred to have a considerable influence, and our empirical fit based on the mean GCDN may become questionable.

The scatterplot of the relative difference between I_0 and I_1 versus the mean GCDN is displayed in Figure 7a. We note that the distribution is one-sided (i.e., I_1 is always larger than I_0). This is understandable based on the nature of the RGB "saturated" response (see also the Supplementary Materials): Under time-varying auroras, the averaged response is biased toward the lower auroral intensity epochs. In this regard, it is true that by using the mean GCDN over the TRSp integration time, we might somehow overestimate the nonlinear slope of the RGB response. That said, the

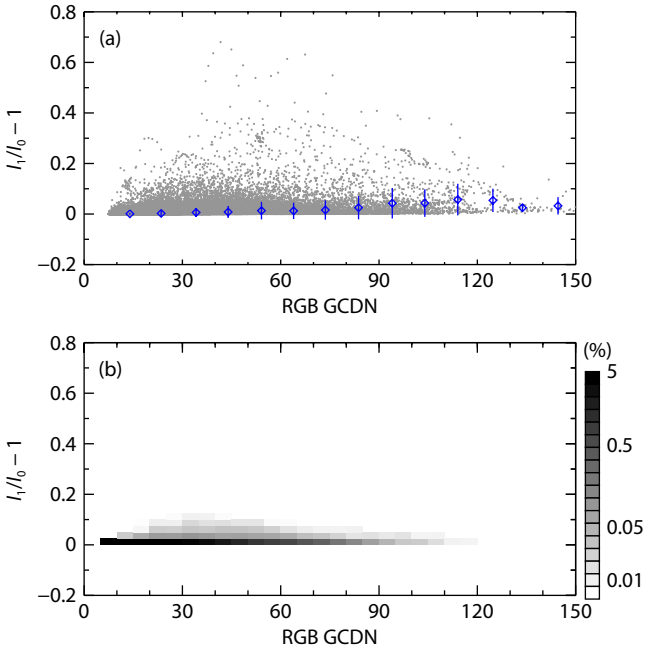

Figure 7. (a) Scatterplot of the relative difference between I_0 and I_1 (see text for details). The blue diamonds and lines indicate the mean and standard deviation of the relative difference in successive GCDN bins beginning at 10, with each having a width of 10. (b) The density distribution corresponding to the scatterplot (a).

difference is not significant. Following the approach depicted above, in Figure 7a we overplot the mean and standard deviation of the relative difference in successive GCDN bins, each with a width of 10. Figure 7b shows the density plot of the relative difference. As one can infer, the distribution is narrowly confined to near zero up to a GCDN of ~110; the probability of occurrence drops by more than an order of magnitude beyond a relative difference of a few percent. At a GCDN of greater than ~110, the data points become relatively fewer and scattered, and the statistics become less robust there. In a statistical sense, the difference between I_0 and I_1 tends to be much smaller than the scatter of the original data points led by other error sources (e.g., the photon shot noise and the elevation-angle dependence of the conversion ratios). To conclude, uncertainty led by the fine-scale time variation of auroras does exist, but the resultant error of the empirical fit in our procedure based on the mean GCDN over the TRSp integration time is not significant, considering the presence of other error sources and the allowed uncertainty margin of the present study.

3.2 Calibration with In Situ Particle Measurements and the TREx-ATM

It is, of course, desirable to have collocated optical instruments that provide realistic measurements of the green-line auroral intensity for the RGB calibration, but this is not always available. For the presently deployed TREx-RGB ASI stations, the TRSp exists only at RABB and LUCK. For the rest of the RGB ASIs, other methods must be summoned to evaluate the 557.7 nm auroral intensity. In this subsection, we demonstrate the approach based on the TREx-ATM calculation with realistic electron precipitation flux data from the Defense Meteorological Satellite Program (DMSP) satellite passing over the ASI FoV. The TREx-ATM is the support model of the TREx mission. The model is designed to simulate the transport of auroral electrons in the upper atmosphere, including impact ionization and secondary electron production, as well as the impact excitation of neutrals. The model computes the photon volume emission rates (VERs) of optical auroras at various wavelengths in response to electron precipitation inputs. The excitation cross sections and the numerical scheme (two-stream approximation) to solve the electron transport equation are essentially inherited from the GLOW (GLobal airglOW) model (Solomon et al., 1988; Solomon, 2017), with a few notable advances:

(1) Changes in plasma density and temperature, as well as temperature-dependent reaction rates, are self-consistently calculated in the TREx-ATM.
(2) The model can be time dependent, although only the steady-state solution is used in this study.
(3) A number of the reaction coefficients are updated.

For more details on the model and updated reaction or excitation rates, see Liang J et al. (2016, 2017, 2021). Comprehensive production or loss mechanisms of 557.7 nm emissions are considered in the model, including the direct-impact excitation of O and the reaction of $N_2(A)$ + O (e.g., Shepherd and Shepherd, 1995; Whiter et al., 2023). Note that we use the RABB ASI in the following event example; our goal in this work is to demonstrate the procedures and validate the credibility of the ATM-based approach by comparison with the conversion factor derived with TRSp measurements, to pave the way toward a more dedicated use of the approach in the future. We wish to clarify that the ATM-modeled 557.7 nm intensity is understandably subject to more uncertainties than the realistically measured one. In addition, favorable passages of low-Earth-orbit (LEO) satellites are not common. Low-Earth-orbit satellites that can measure the electron precipitation of flux spectra have been relatively scarce in recent years, and the number of usable data points in one passage is limited. Therefore, in the following event example, we shall be contented with the evaluation of an overall linear conversion ratio between the GCDN and the modeled 557.7 nm intensity. Intensity-dependent conversion may be done when we assemble a sizable pool of LEO satellite passage events in the future.

Figure 8a demonstrates the RABB RGB images (dark/background subtracted) overplotted with the footprint trajectory of the DMSP F18. Figure 8b displays the electron energy flux spectrogram measured by the Special Sensor J (SSJ) instrument onboard the F18 for this passage. We simulate, based on DMSP SSJ data on electron precipitation fluxes, the green-line auroral intensities with the TREx-ATM. Here, we highlight two additional procedures that were not documented in previous publications but are important for the specific purpose of this study, namely, to make a quantitative comparison between the ATM outcome and the ground optical measurement.

First, the optical intensity received by a ground imager represents an integral of the VER along the LOS direction. In this study, to properly simulate the auroral intensity seen by a ground imager, we take into account the oblique observational geometry and perform an LOS integral of the VER at each elevation angle. This

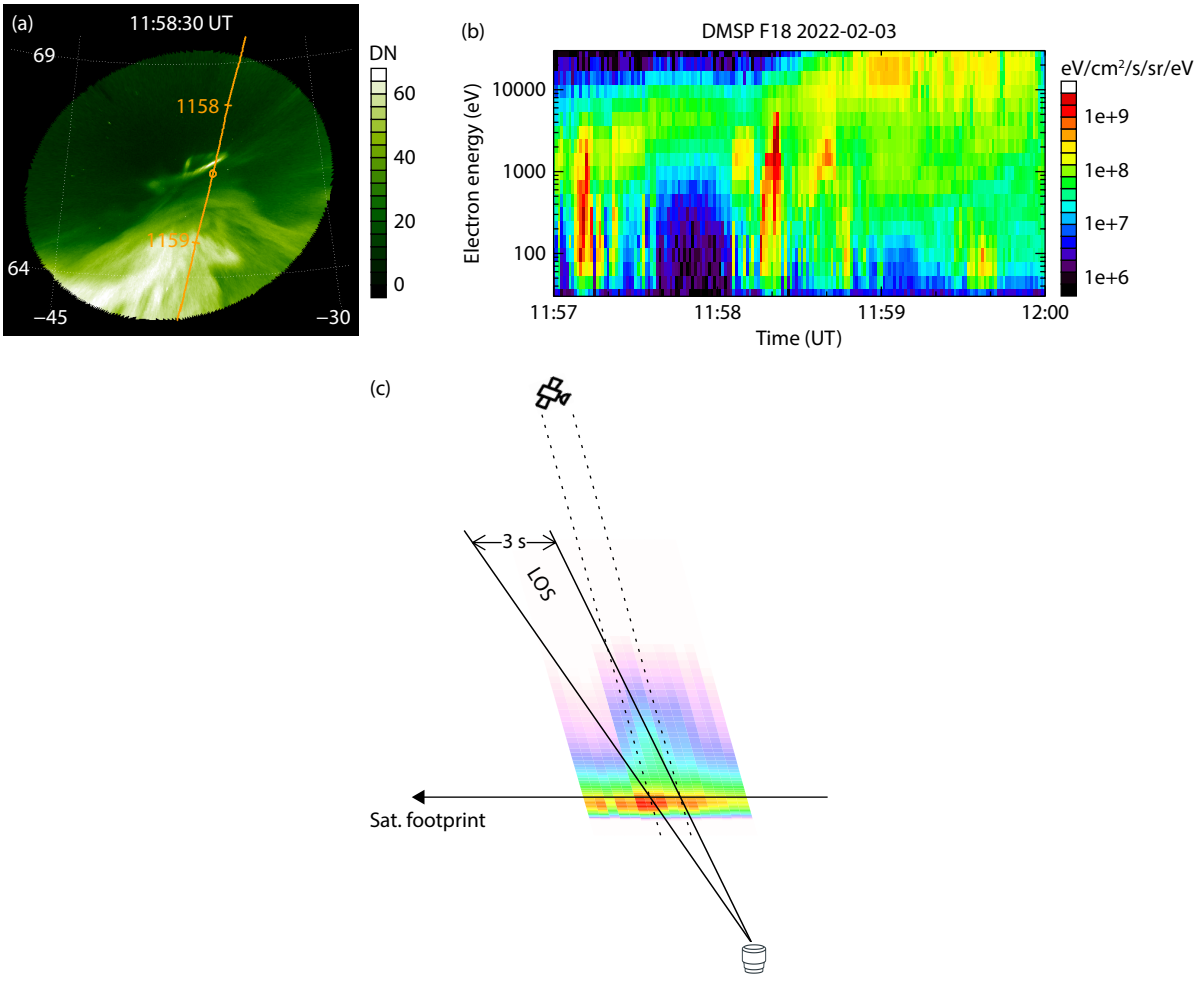

Figure 8. (a) An example of the RGB green-channel image taken on February 3, 2022, at 11:58:30 UT. The DMSP F18 footprint trajectory is overplotted as an orange line. An orange circle marks the location of the satellite footprint at the image epoch. (b) The DMSP SSJ electron energy flux spectrogram for the passage. (c) Schematic diagram illustrating the geometry and our procedures for sampling the along-track RGB GCDN and for calculating the corresponding 557.7 nm auroral intensities from the TREx-ATM. The VERs calculated from the TREx-ATM based on SSJ flux data from 11:58:32 to 11:58:48 UT are plotted. Two oblique solid lines denote the elevation angle range of satellite footprints over a 3-s image interval. Two dotted lines exemplify the magnetic field lines.

process requires knowledge of the spatial distribution of the electron precipitation, which we infer from the DMSP observations, and assumptions regarding the temporal–spatial ambiguity inherent in satellite measurements. Figure 8c shows a diagram demonstrating the procedure we use to sample and calculate the along-track auroral intensities measured by the RGB ASI and those that were computed by the TREx-ATM with SSJ electron precipitation input. The figure is mainly intended to be a schematic diagram, but the magnetic latitude (mlat)–altitude distribution of the VER calculated from the realistic SSJ electron fluxes from 11:58:32 to 11:58:48 UT is plotted to assist the presentation. For each SSJ electron precipitation input of 1-s cadence, the resulting VER along the corresponding field line (exemplified by the dotted lines in Figure 8c) is computed. For each 3-s cadence of the RGB ASI, we determine the elevation angle range of the satellite footprint during this 3-s interval (marked by two oblique solid lines in Figure 8c) according to the positions of the satellite footprint. The satellite footprint is evaluated at an altitude of 110 km; the uncertainty of this specification does not have a significant influence on our results because of the LOS integral involved in our algorithm. We sample and average the RGB ASI GCDN values of the 3-s frame in the elevation angle range above. We also calculate and average the ATM-simulated, LOS-integrated 557.7 nm intensity within the same elevation angle range by using the 1-s cadence SSJ electron flux data. The computation of the latter under oblique geometry would not only require the electron precipitation data during the current 3-s interval, but also would involve SSJ data from the nearby seconds to construct a spatial distribution of the VER for the LOS integral. One key assumption in this regard is that the electron precipitation is assumed to be essentially non-time-varying over the period of ~10 s so that the satellite observations can be deemed dominantly representing the mlat distribution of electron precipitation over this period. This assumption certainly has limitations and may become problematic under circumstances of highly dynamic auroras (e.g., in the case of pulsating auroras), but the approach described above reflects our best effort to date in simulating the imager view of auroral intensities under oblique geometry based on available data. Because the viewing direction

of the satellite is not meridional, we have also assumed a local mlon homogeneity of electron precipitation around the satellite track and allowed for 0.4° mlon full width in sampling the RGB GCDN around the satellite footprint.

Second, the auroral light is subject to atmospheric attenuation before it reaches a ground imager. The atmospheric attenuation of optical lights is wavelength dependent. The 557.7 nm emission of interest belongs to the "pass window" of the atmosphere such that the attenuation is not severe unless clouds prevail, but the light may still undergo Rayleigh scattering in the atmosphere as well as aerosol extinction. The attenuation is also dependent on the elevation angle, which determines the LOS path length in the atmosphere. In simplified form, the atmospheric attention can be characterized by the atmospheric optical depth τ, and the attenuation factor is given by

$$A = \exp\left(-\frac{\tau}{\sin\alpha}\right), \tag{3}$$

in which α is the elevation angle of the LOS direction. To evaluate the atmospheric optical depth, we adopt the model previously built for a separate SMILE-related project, in which we evaluated the influence of solar scattering on the SMILE Ultraviolet Imager (Liang J et al., 2019c) based on the simplified radiative transfer model of Seidel et al. (2010). We take into consideration Rayleigh scattering and aerosol extinction but no clouds. Using a standard MODTRAN (MODerate resolution atmospheric TRANsmission) subarctic winter atmosphere and an OPAC (Optical Properties of Aerosols and Clouds) continental clean aerosol profile, we obtain a total optical depth of $\tau \sim 0.16$ for the 557.7 nm wavelength of interest, a value to be used in the following calculation. We note that this optical depth value is compatible with what is achieved or presented in existing publications (e.g., see Fig. 2 in Kopparla et al., 2018, and Fig. 5 in Shiobara et al., 1996).

The black curve in Figure 9a shows the simulated 557.7 nm optical intensity along the DMSP footprint trajectory as received by the ASI, taking into account the LOS integral and the atmospheric attenuation. The TREx-RGB GCDN sampled along the DMSP trajectory is shown by the green curve. Figure 9b shows the scatterplot of the sampled along-track GCDN and the ATM-simulated 557.7 nm intensity. In both Figures 9a and 9b, the part where the zenith angle is within 60°, which is our main analysis of interest, is highlighted with thickened lines or circles. As can be seen in Figure 9b, the along-track GCDN and ATM-simulated 557.7 nm intensity show an approximately linear relation for a zenith angle <60° and a 557.7 nm intensity <20 kRa. A linear fit in this range yields a linear coefficient of 310 (±43), which is used in Figure 9a to scale the GCDN. Reasonable agreement is achieved between the along-track GCDN and the simulated 557.7 nm aurora intensities for zenith angles <60°. A conversion ratio of ~310 between the GCDN and the 557.7 nm intensity is thus estimated by the ATM-based approach. Later in this passage, the satellite enters a region dominated by pulsating auroras, as can be inferred from the oscillatory pattern of both the SSJ electron fluxes (Figure 8b) and the along-track GCDN (Figure 9a) after 11:59 UT. The apparent auroral intensities there are strong, so the conversion ratio is presumed to be larger than that for moderate auroras in earlier times owing to the nonlinear RGB response, but we shall not

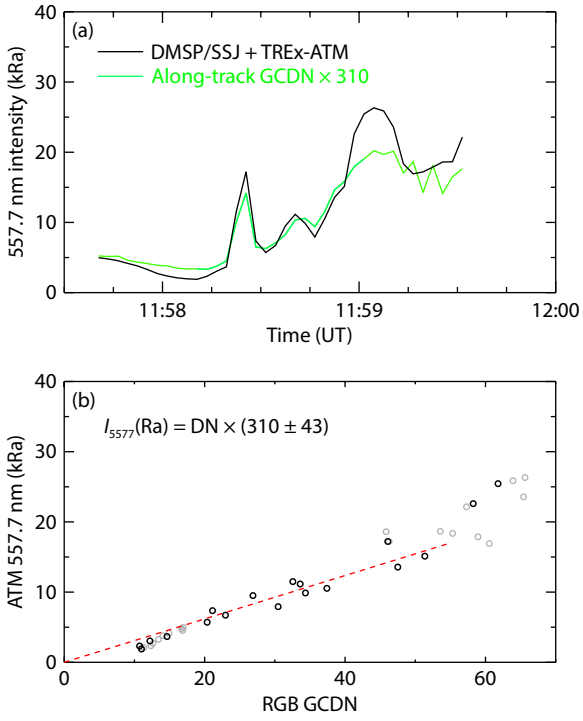

Figure 9. (a) The black curve shows the simulated 557.7 nm optical intensity along the DMSP footprint trajectory as received by the ASI. The green curve shows the TREx-RGB GCDN sampled along the DMSP trajectory scaled by a factor of 310. (b) Scatterplot of the sampled along-track GCDN and the ATM-simulated 557.7 nm intensity. The red dashed line marks the best linear fit, whose coefficient is used in (a). In both (a) and (b), the part where the zenith angle is <60°, which is our main analysis of interest, is highlighted with thickened lines or circles.

pursue the conversion factor further for the pulsating aurora structures for the following reasons:

(1) These auroras occur at large zenith angles (>60°) toward the south, beyond the intended range of this study.
(2) More important, as mentioned, our algorithm for constructing the spatial distribution of electron precipitation from the DMSP assumes that the DMSP observations during the passage of an auroral structure represent only the mlat distribution of the structure, yet it neglects the temporal fluctuation. This may become problematic in the case of pulsating auroras, such that large errors in our model calculation are expected there.

We note that the linear conversion factor inferred from the TREx-ATM approach seems to be higher overall than that inferred from the TRSp (~269 ± 40) during the same time interval (see Figure 5d), yet their difference is within the allowed error margin (~20%) of this study. Such a discrepancy is not unexpected. The TREx-ATM calculation is subject to the uncertainties of reaction coefficients, excitation cross sections, and atmospheric optical depths. Furthermore, because the event occurred during the main phase of a moderate storm ($Dst \sim -66$), the storm-associated neutral upwelling might have caused the atomic oxygen density in the lower thermosphere to be lower than that in the empirical neutral model used in our calculation (e.g., Zhang YL et al., 2004, 2014), so our model might somehow overestimate the OI 557.7 nm intensity

because of the higher-than-actual model oxygen density. Currently, the empirical neutral model we adopt is NRLMSIS 2.0 (Emmert et al., 2021), which is supposed to better depict the storm-time thermosphere (parameterized by historical *Ap* indexes) than previous versions. Using the NRLMSIS-00 (Picone et al., 2002) instead, we obtain an even higher model 557.7 nm intensity and, in turn, a higher conversion ratio of ~322 ± 45. We thus infer that the empirical neutral density model does impose an uncertainty for our GCDN conversion ratio estimate. We wish to emphasize that the TREx-ATM is still a developing model, and it is our plan to improve it with calibrated TREx data in the near future. Some of the planned model advances are discussed in Section 3.3. Nevertheless, we expect, based on the result achieved from this example, that for RGB stations without collocated 557.7 nm measurements, the TREx-ATM may offer a way to estimate the approximate GCDN-to-Rayleigh conversion factor within an acceptable error margin (~20% as our intended target).

3.3 LUCK RGB Calibration with the TRSp

The analyses above are focused on the TREx-RGB at RABB. We have also made similar analyses on the RGB ASI at LUCK, Canada. Unlike RABB, LUCK (~59° mlat) is in the subauroral region; in most cases, auroral activities were either absent or existed only near the northern edge of the ASI FoV. The LUCK ASI and TRSp were mainly used to study the subauroral optical phenomena, such as SAR (stable auroral red arcs) and STEVE (strong thermal emission velocity enhancement; e.g., Gillies et al., 2019, 2020, 2023; Liang J et al., 2019b). That said, under certain circumstances, bright auroras might also be active in the LUCK ASI FoV: (1) during a strong geomagnetic disturbance when the equatorward boundary of the auroral oval had moved substantially southward; or (2) in the presence of isolated proton auroras (IPAs, e.g., Sakaguchi et al., 2007; Gallardo-Lacourt et al., 2021). For example, on the night of October 12, 2021 (known as the Canada Thanksgiving storm), intense IPAs occurred and were visible to citizen scientists over western Canada (Liang J et al., 2022; Nishimura et al., 2022). An IPA is led by proton precipitation, yet 557.7 nm constitutes the strongest emission line of the IPA (Sakaguchi et al., 2007; Liang J et al., 2022). For that reason, we collect the collocated RGB ASI and TRSp measurements at LUCK over 7 h on two geomagnetic storm nights when strong auroras prevailed over the LUCK ASI FoV: (1) 03:00–05:00 UT, 06:00–07:00 UT, and 10:00–11:00 UT on October 12, 2021, and (2) 06:00–09:00 UT on November 4, 2021. Following the same procedures as depicted in Section 3.1, we present in Figure 10a the scatterplot of the sampled RGB GCDN and TRSp 557.7 nm intensity at LUCK. Figure 10b shows the density plot of the collected data points in the same format as in Figure 6b. Again, we overplot the mean and standard deviation of the 557.7 nm intensities in successive GCDN bins, each with a width of 10 (Figure 10a), to help readers discern the general trend of the response.

As one can see, the response of the LUCK RGB GCDN to the 557.7 nm intensities is similar overall to that for the RABB RGB ASI (see Figure 6a). The response is quasi-linear at low to moderate intensities yet becomes nonlinear at high intensities. Upon careful comparison between Figures 10a and 6a, we find that the nonlinear trend begins to become noticeable at somewhat lower GCDN

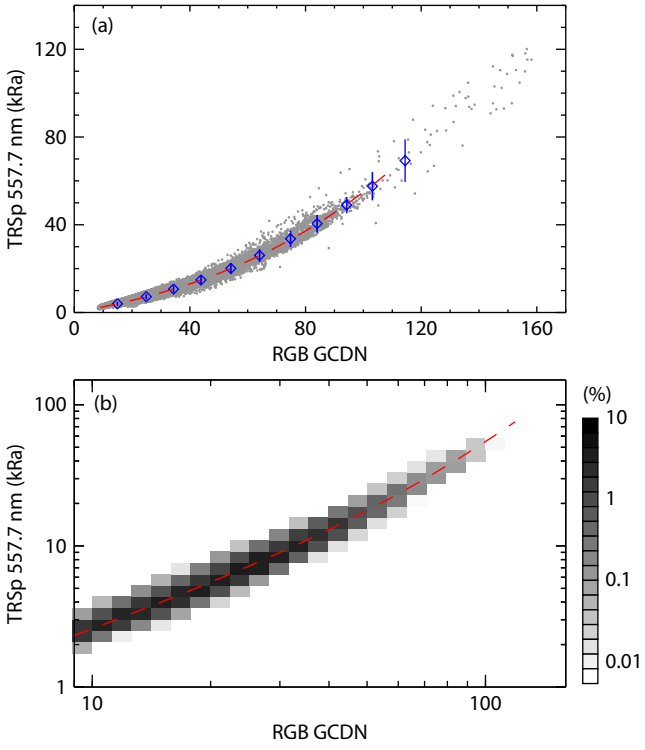

Figure 10. The same format and legends as in Figure 6, but for the LUCK RGB ASI and TRSp. The red dashed curve denotes the empirical fit according to Equation (4).

values (~50) on the LUCK RGB than on the RABB RGB. Using the criteria put forth in Section 3.1, we find that the quasi-linear condition holds up to only the [40, 50] GCDN bin for the LUCK RGB. We perform a linear fit for data points with GCDN values of <50 and achieve 302 ± 38 as the best-fit linear conversion factor for this range. For a better evaluation at higher intensities, we again perform a fit to the data over the GCDN range [8, 110], where the data points are mostly concentrated:

$$I_{5577}\,(\mathrm{Ra}) = a_1 \cdot \mathrm{GCDN} \cdot \left(1 + a_2 \cdot \mathrm{GCDN}^{a_3}\right), \tag{4}$$

$$a_1 = 249.051,\ a_2 = 1.322 \times 10^{-3},\ a_3 = 1.480.$$

Comparing Equation (4) with Equation (2), the empirical formula for the LUCK RGB ASI has a larger nonlinear term, so the nonlinear trend of the LUCK RGB response begins to prevail at lower GCDN values than that for the RABB RGB ASI. At present, we do not recommend using the empirical formula above beyond a GCDN of ~120, where the data points collected in this study become relatively scarce and scattered. More intense auroral events at LUCK are to be analyzed in the near future to establish a more robust empirical formula that may be applicable at very high auroral intensities.

4. Discussion

We have elucidated the procedures used to calibrate TREx-RGB green-channel data into the absolute green-line auroral intensity and have presented the initial results for the RGB ASIs at RABB and LUCK. We have demonstrated two approaches to evaluate the conversion factors, one based on the collocated TRSp measurements, and the other based on TREx-ATM and LEO satellite

measurements of electron precipitation fluxes. More focus is put on the first approach. Empirical conversion ratios or formulas between the GCDN and the 557.7 nm auroral intensity are given and can be applied immediately by TREx-RGB data users to obtain 2-D time-varying images of the 557.7 nm auroras in their studies. The GCDN response to the green-line emission is nonlinear, but for many practical research purposes, it can be deemed quasi-linear for GCDN values < ~60 for RABB RGB or < ~50 for the LUCK RGB. One of the main reasons for such a nonlinear response at high auroral intensities is presumably due to the saturation of the CMOS sensor adopted for the TREx-RGB.

Although some definitive results are achieved, corroborating the promising use of the TREx-RGB GCDN as a quantitative proxy for the green-line auroral emission, the present study has several limitations. These limitations are pertinent to instrumental issues, the current operational plan, and the model uncertainty. In the following paragraphs, we address these limitations and possible ways to improve the calibration and the accuracy of conversion in the future for both the TREx and the upcoming SMILE ASI.

The uncertainty of this study first comes from the determination of the dark/background frame for subtraction. This will also be one of the challenges for TREx-RGB ASI data users in an effort to use the data for quantitative purposes. In this study, we select quiescent intervals not far away from the event time of interest and adopt a histogram approach to obtain the dark/background value of each ASI pixel. This procedure is not without uncertainty, as discussed in Section 2.2. To partly relieve such uncertainty, in our RGB data selection and collection, data points with a GCDN below 2 times the dark/background value are excluded. From all the intervals we collected, we infer that we achieved a dark/background GCDN average at ~8.76 ± 0.93 for the RABB ASI and ~8.64 ± 0.25 for the LUCK ASI. These values can be used as a reasonable guess of the dark/background values for RGB data users in a process of quick event browse or selection. As a consequence of our data selection criteria, very few data points are collected at a GCDN of <9, as can be seen from the scatterplot (Figures 6a and 10a). As addressed in Section 2.2, the present study may not be applicable to weak auroras (< ~2 kRa), such as the ambient diffuse aurora. In the future, we shall consider using an external shutter to do dark frame shooting on a regular basis (e.g., once every night) for the TREx-RGB ASI operation. We also recommend that in the future operation of the SMILE ASI, dark frames be taken regularly.

Uncertainty also exists at very high intensity auroras. In the empirical fit performed in this study, we have limited the fitting range to where the data points are reasonably abundant. Data points at very high intensities of 557.7 nm (> ~60 kRa) collected in this study are relatively scarce and scattered and are not suitable for robust statistical analysis. This situation should be improved when we are able to collect more of the extremely strong auroral events in the future, which is presumably achievable with the approaching solar maximum. Furthermore, it is reasonable to consider that events with very high auroral intensities usually belong to the most active periods and are supposed to be highly dynamic. As discussed in Section 3.1, strong and rapidly time-varying auroras with timescales much smaller than the TRSp integration time may impose errors in the determination of conversion factors when using time-averaged RGB and TRSp data. Last but not least, the TRSp measurement itself might also become problematic at very high auroral intensities. We have used NIST standard low-brightness light to obtain the calibration factor to convert the raw TRSp digital number to the spectral intensity. In using this procedure, we have assumed that the TRSp response is always linear, which might become questionable at very high auroral intensities. Upon closer look at Figures 6a and 10a, one may notice that, notwithstanding the scarcity of data points with GCDN values beyond ~90–100, a marginal trend seems to exist in the change of "concavity" (the second derivative), which might arguably allude to the possible "saturation" of TRSp data at extreme auroral intensities. The TRSp uses a CCD as the imaging sensor. A high-level scientific CCD often has a higher dynamic range and better linearity than a CMOS. As per consultation with the CCD manufacturer (Andor, private communication), as the manufacturing standard, the Andor CCD in use is expected to maintain 99% linearity up to at least ~60% of the full dynamic range. In this regard, we have checked the spectrograph raw signal data and found that the postulated linearity limit was never reached, even during the strongest auroral event we collected. We note, however, that the manufacturing standard is better considered a reference rather than a guarantee for individual instruments. Furthermore, other optical components of the TRSp, such as the collimator and the diffraction grating, might also be subject to nonlinear optical effects under strong light input. Therefore, although we do expect that the linearity of the TRSp extends to much higher auroral intensities than that of the TREx-RGB, the possibility of a nonlinear TRSp response at very strong intensities cannot be dismissed outright. Extreme auroral events are, of course, rare, but when they occur, they are usually of keen research interest and associated with the most severe space weather effects. More accurate conversion between the GCDN and 557.7 nm intensities under very strong auroral conditions is thus a desirable task. To achieve this, laboratory measurements of the nonlinear response of both the TREx-RGB and TRSp with standard light sources are required, which we tentatively plan to begin in early 2024.

We have also demonstrated the use of the TREx-ATM with realistic in situ electron flux data to model the 557.7 nm intensity and, in turn, estimate the conservation ratio for the RGB GCDN, which is our intended approach for TREx-RGB stations without collocated optical instruments to measure the green line. Understandably, the ATM-modeled 557.7 nm intensity and, in turn, the conversion ratio based on the model intensity are subject to more uncertainties than that with the realistically measured green-line intensity. In the example we demonstrated, the conversion ratio based on the ATM approach is slightly larger overall than that based on TRSp measurements during the same event interval. The TREx-ATM is subject to uncertainties in the reaction coefficients, excitation cross sections, and atmospheric attenuation. Furthermore, green-line auroral intensities have a nontrivial dependence on the neutral O density (e.g., Shepherd et al., 1995; Grubbs et al., 2018). Since the demonstrated event occurred during the SpaceX geomagnetic storm interval when significant neutral upwelling was known to occur and caused damage to satellites, we speculate that the O density may somehow differ from that in the NRLMSIS

2.0 empirical model we used in our calculation, leading to errors of OI 557.7 nm intensities in our model. In future advances of the TREx-ATM, it is highly desirable to evaluate and adjust the neutral density according to realistic data from individual events. For example, the 844.6 nm near-infrared emission is known to be sensitive to the atomic O density and can be used to infer the dynamic change of O densities during active intervals (Hecht et al., 1989, 2006; Strickland et al., 1989), which is the reason we include it in the TREx system. There are existing efforts to estimate the adjustment factor for the O/N_2 column density ratio based on multi-wavelength optical measurements (e.g., Hecht et al., 1989, 2006; Zhang YL et al., 2004; Grubbs et al., 2018). It is our plan to use calibrated TREx observations, including the multi-wavelength (427.8/630/844.6 nm) imagers and RGB ASIs, to evaluate the O/N_2 ratio and apply such an adjustment in the TREx-ATM for more accurate modeling of the relevant auroral intensities. In the meantime, we are now collecting more and more events with LEO satellite passages over the FoV of the TREx-RGB ASIs. The model advances and the accumulation of the satellite passage database proceed in parallel, and more refined analyses using TREx-ATM and LEO satellite data to evaluate conversion ratios for TREx-RGB ASIs will be conducted in the near future. We expect that the improved TREx-ATM will also become the main support model of the SMILE ASI mission and will be involved in future calibration of the SMILE ASIs.

5. Summary and Conclusions

The TREx mission deployed by the University of Calgary, Canada, is dedicated to monitoring the spatiotemporal variations of auroras in the nightside transition region with ground-based network observations, including multi-wavelength optical imagers and imaging riometers. The TREx datasets are to be used to infer the dynamic changes in magnetosphere–ionosphere coupling that drive the auroras, as well as to remote-sense the associated particle energization and transport processes in the near-Earth magnetosphere. The 557.7 nm green line, typically the strongest emission line of visible auroras, is of great importance to the mission objective. However, the current deployment of the TREx does not include a specific green-line imager and resorts to the RGB green channel as a proxy for the green-line emission. The upcoming SMILE ASI mission to be deployed by the University of Calgary, Canada, will also adopt RGB cameras and follow the same strategy. In this work, we take the first step in investigating the feasibility of using RGB data to infer the absolute green-line auroral intensity. We demonstrate the procedures and provide initial results for the RGB ASIs at RABB and LUCK. These results and the recommended procedures or parameters for TREx users to convert the RGB GCDN values into 557.7 nm intensities are summarized as follows.

The first necessary procedure is proper dark/background subtraction. At present, no dark frame shooting is done by the TREx-RGB. Viable procedures to construct the dark/background frame of the green channel have been proposed and demonstrated in this paper. For users who wish to do quick event browsing or selection and are contented with a rough estimation of the 557.7 nm intensities without efforts to construct the dark/background frame, ~9 can be assumed as a guess of the dark/background GCDN value for both the RABB and LUCK ASIs for expedited data processing. The results of this study may not apply to very weak auroras (< ~2 kRa). For the future operation of the TREx-RGB and SMILE ASIs, we consider doing dark frame shooting on a regular schedule (e.g., once per night).

After the dark/background subtraction, for low to moderate GCDN values (<60 for RABB and <50 for LUCK), a linear conversion ratio of ~280 (~300) Ra per digital number can be used for the RABB (LUCK) ASI. This ratio would suffice for many practical research purposes, particularly if the users are content with an approximate estimation of the 557.7 nm intensity. For more accurate conversion ratios, especially at higher GCDN values, the empirical formulas in Equations (2) and (4) can be used for the RABB and LUCK ASIs, respectively. However, caution needs to be exercised when using these formulas at very strong 557.7 nm auroral intensities, for the reasons discussed in the last section. Conversion of the GCDN to the green line at very high auroral intensities needs to be further examined in the future. At present, we are conservative in recommending using the empirical formulas described above for GCDN values greater than ~120 for both the RABB and LUCK ASIs. Finally, recall again that the derived conversion ratios in this study should be deemed the mean over 30°–150° elevation angles of the ASI. At present, preliminary evaluation based on a large number of auroral images hints that the flat-field variability might not be too significant to invalidate the results of this study. Pixel-to-pixel variations in the conversion ratio, as well as the extension to lower elevation angles, will be investigated once the flat-field calibration of the TREx-RGB ASI is accomplished.

We have also demonstrated the use of the TREx-ATM with input from in situ electron precipitation flux measurements to evaluate the conversion ratio between the GCDN and the green-line intensity. This will be the planned method for TREx-RGB stations without a collocated TRSp. Through the event exemplified in this paper, we find that such an ATM-based approach, despite having larger uncertainty than that with realistic 557.7 nm intensity measurements, can nevertheless offer an estimate of the conversion ratio within a reasonable error margin. The TREx-ATM is being tuned and improved with accumulating TREx datasets. The conversion ratios for the rest of the TREx-RGB ASIs will be evaluated with the TREx-ATM and published in the near future.

Although tasks are needed for future refinement and advancement, the results achieved in this study have definitely confirmed the promising potential of using RGB data as a quantitative proxy for the green-line auroral emission. Not only is this result of crucial importance to the current TREx mission, but it is also encouraging and instructive for the upcoming SMILE ASI mission. The methodology established in this study is also applicable to the upcoming SMILE ASIs.

Acknowledgments

The TREx is jointly funded by the Canada Foundation for Innovation, the Alberta Economic Development and Trade organization, and the University of Calgary. The TREx-ATM is supported by the Canadian Space Agency. The TREx-RGB and spectrograph data can be found at https://data.phys.ucalgary.ca/sort_by_project/

TREx/. The DMSP SSJ data were downloaded from http://cedar.openmadrigal.org.

Supplementary Materials

In this appendix, we provide a simple mathematical analysis of the error of our empirical fit led by fluctuating auroras within the TRSp integration time and the nonlinear RGB response, and why the relative difference between I_0 and I_1 (see text for details) can be used to semi-quantitatively evaluate such an error. Ignoring all other error or noise sources, we assume that the "true" relation between the 557.7 nm intensity and the GCDN is given by

$$I = f_{\rm tr}(G), \tag{A1}$$

in which I denotes the 557.7 nm intensity and G denotes the GCDN, considering a time-varying aurora with intensity $I(t)$ and the resultant RGB response $G(t)$. The mean 557.7 nm intensity and the CGDN over the integration time are denoted by $\bar{I} = \overline{f_{\rm tr}[G(t)]}$ and $\bar{G} = \overline{G(t)}$, respectively. In making our empirical fit, we use the mean 557.7 nm intensity and CGDN,

$$\bar{I} = f_{\rm mn}\left(\bar{G}\right). \tag{A2}$$

Comparing Equations (A1) and (A2), we have

$$f_{\rm mn}\left(\bar{G}\right) = \overline{f_{\rm tr}(G)}. \tag{A3}$$

When $f_{\rm tr}$ is nonlinear, the function form $f_{\rm mn}$ of our empirical fit differs from $f_{\rm tr}$. To better elucidate this, we perform a Taylor expansion of $f_{\rm tr}(G)$ around $\bar{G}$,

$$f_{\rm tr}(G) = f_{\rm tr}\left(\bar{G}\right) + \left.\frac{\partial f_{\rm tr}}{\partial G}\right|_{\bar{G}} \cdot \left(G-\bar{G}\right) + \frac{1}{2}\left.\frac{\partial^2 f_{\rm tr}}{\partial G^2}\right|_{\bar{G}} \cdot \left(G-\bar{G}\right)^2, \tag{A4}$$

where we have

$$f_{\rm mn}\left(\bar{G}\right) = f_{\rm tr}\left(\bar{G}\right) + \frac{1}{2}\left.\frac{\partial^2 f_{\rm tr}}{\partial G^2}\right|_{\bar{G}} \cdot \overline{\left(G-\bar{G}\right)^2}. \tag{A5}$$

In the realistic case that $f_{\rm tr}$ is monotonically increasing yet G has a trend of saturation toward high I, $\frac{\partial^2 f_{\rm tr}}{\partial G^2} > 0$, we have $f_{\rm mn}(G) > f_{\rm tr}(G)$.

Following the definition in the text, we construct the I_0 and I_1 according to formula (A2),

$$I_0 = f_{\rm mn}\left(\bar{G}\right) = \overline{f_{\rm tr}(G)}, \tag{A6}$$

$$I_1 = \overline{f_{\rm mn}(G)}. \tag{A7}$$

We have used Equation (A3) in Equation (A6). The difference between I_0 and I_1 is thus

$$I_1 - I_0 = \overline{f_{\rm mn}(G) - f_{\rm tr}(G)}. \tag{A8}$$

The right-hand side of Equation (A8) denotes the mean difference between the "true" function and the "mean" function over the integration time. In this sense, we infer that the difference between I_0 and I_1 can be used as an approximate gauge of the error of our empirical fit (in using the mean 557.7 nm intensity and GCDN) with respect to the true relation.

References

Baker, K. B., and Wing, S. (1989). A new magnetic coordinate system for conjugate studies at high latitudes. *J. Geophys. Res.: Space Phys.*, *94*(A7), 9139–9143. https://doi.org/10.1029/JA094iA07p09139

Branduardi-Raymont, G., Wang, C., Escoubet, C. P., Adamovic, M., Agnolon, D., Berthomier, M., Carter, J. A., Chen, W., Colangeli, L., … Zhu, Z. (2018). SMILE definition study report. European Space Agency.

Emmert, J. T., Drob, D. P., Picone, J. M., Siskind, D. E., Jones, M., Mlynczak, M. G., Bernath, P. F., Chu, X., Doornbos, E., … Yuan, T. (2021). NRLMSIS 2.0: A whole-atmosphere empirical model of temperature and neutral species densities. *Earth Space Sci.*, *8*, e2020EA001321. https://doi.org/10.1029/2020EA001321

Gabrielse, C., Nishimura, T., Chen, M., Hecht, J. H., Kaeppler, S. R., Gillies, D. M., Reimer, A. S., Lyons, L. R., Deng, Y., … Evans, J. S. (2021). Estimating precipitating energy flux, average energy, and hall auroral conductance from THEMIS all-sky-imagers with focus on mesoscales. *Front. Phys.*, *9*, 744298. https://doi.org/10.3389/fphy.2021.744298

Gallardo-Lacourt, B., Frey, H. U., and Martinis, C. (2021). Proton aurora and optical emissions in the subauroral region. *Space Sci. Rev.*, *217*, 10. https://doi.org/10.1007/s11214-020-00776-6

Gillies, D. M., Knudsen, D., Donovan, E., Jackel, B., Gillies, R., and Spanswick, E. (2017). Identifying the 630 nm auroral arc emission height: A comparison of the triangulation, FAC profile, and electron density methods. *J. Geophys. Res.: Space Phys.*, *122*(8), 8181–8197. https://doi.org/10.1002/2016JA023758

Gillies, D. M., Donovan, E., Hampton, D., Liang, J., Connors, M., Nishimura, Y., Gallardo-Lacourt, B., and Spanswick, E. (2019). First observations from the TREx spectrograph: The optical spectrum of STEVE and the picket fence phenomena. *Geophys. Res. Lett.*, *46*(13), 7207–7213. https://doi.org/10.1029/2019GL083272

Gillies, D. M., Liang, J., Donovan, E., and Spanswick, E. (2020). The apparent motion of STEVE and the picket fence phenomena. *Geophys. Res. Lett.*, *47*(20), e2020GL088980. https://doi.org/10.1029/2020GL088980

Gillies, D. M., Liang, J., Gallardo-Lacourt, B., and Donovan, E. (2023). New insight into the transition from a SAR arc to STEVE. *Geophys. Res. Lett.*, *50*(6), e2022GL101205. https://doi.org/10.1029/2022GL101205

Grubbs, G., Michell, R., Samara, M., Hampton, D., Hecht, J., Solomon, S., and Jahn, J. M. (2018). A comparative study of spectral auroral intensity predictions from multiple electron transport models. *J. Geophys. Res.: Space Phys.*, *123*(1), 993–1005. https://doi.org/10.1002/2017JA025026

Hecht, J. H., Christensen, A. B., Strickland, D. J., and Meier, R. R. (1989). Deducing composition and incident electron spectra from ground-based auroral optical measurements: Variations in oxygen density. *J. Geophys. Res.: Spaces Phys.*, *94*(A10), 13553–13563. https://doi.org/10.1029/JA094iA10p13553

Hecht, J. H., Strickland, D. J., and Conde, M. G. (2006). The application of ground-based optical techniques for inferring electron energy deposition and composition change during auroral precipitation events. *J. Atmos. Sol.-Terr. Phys.*, *68*(13), 1502–1519. https://doi.org/10.1016/j.jastp.2005.06.022

Hu, Z. J., Yang, H., Huang, D., Araki, T., Sato, N., Taguchi, M., Seran, E., Hu, H., Liu, R., … Liu, S. (2009). Synoptic distribution of dayside aurora: Multiple-wavelength all-sky observation at Yellow River Station in Ny-Ålesund, Svalbard. *J. Atmos. Sol.-Terr. Phys.*, *71*(8-9), 794–804. https://doi.org/10.1016/j.jastp.2009.02.010

Jackel, B. J., Unick, C., Syrjäsuo, M. T., Partamies, N., Wild, J. A., Woodfield, E. E., McWhirter, I., Kendall, E., and Spanswick, E. (2014). Auroral spectral estimation with wide-band color mosaic CCDs. *Geosci. Instrum. Method. Data Syst.*, *3*(1), 71–94. https://doi.org/10.5194/gi-3-71-2014

Janhunen, P. (2001). Reconstruction of electron precipitation characteristics from a set of multiwavelength digital all-sky auroral images. *J. Geophys. Res.: Space Phys.*, *106*(A9), 18505–18516. https://doi.org/10.1029/2000JA000263

Kopparla, P., Natraj, V., Crisp, D., Bott, K., Swain, M. R., and Yung, Y. L. (2018). Observing oceans in tightly packed planetary systems: Perspectives from polarization modeling of the TRAPPIST-1 system. *Astron J*, *156*(4), 143. https://doi.org/10.3847/1538-3881/aad9a1

Liang, J., Spanswick, E., Nicolls, M. J., Donovan, E. F., Lummerzheim, D., and Liu, W. W. (2011). Multi-instrument observations of soft electron precipitation and its association with magnetospheric flows. *J. Geophys. Res.: Space Phys.*, *116*(A6), A06201. https://doi.org/10.1029/2010JA015867

Liang, J., Donovan, E., Jackel, B., Spanswick, E., and Gillies, M. (2016). On the 630

nm red-line pulsating aurora: Red-line Emission Geospace Observatory observations and model simulations. *J. Geophys. Res.: Space Phys.*, *121*(8), 7988–8012. https://doi.org/10.1002/2016JA022901

Liang, J., Yang, B., Donovan, E., Burchill, J., and Knudsen, D. (2017). Ionospheric electron heating associated with pulsating auroras: A Swarm survey and model simulation. *J. Geophys. Res.: Space Phys.*, *122*(8), 8781–8807. https://doi.org/10.1002/2017JA024127

Liang, J., Shen, Y., Knudsen, D., Spanswick, E., Burchill, J., and Donovan, E. (2019a). e-POP and red line optical observations of Alfvénic auroras. *J. Geophys. Res.: Space Phys.*, *124*(6), 4672–4696. https://doi.org/10.1029/2019JA026679

Liang, J., Donovan, E., Connors, M., Gillies, D., St-Maurice, J. P., Jackel, B., Gallardo-Lacourt, B., Spanswick, E., and Chu, X. (2019b). Optical spectra and emission altitudes of double-layer STEVE: A case study. *Geophys. Res. Lett.*, *46*(23), 13630–13639. https://doi.org/10.1029/2019GL085639

Liang, J., Spanswick, E., and Donovan, E. (2019c). Models of solar radiation scattering, dayglows, and auroras for SMILE UVI. In *SMILE Modelling Working Group Meeting*. Madrid, Spain.

Liang, J., St-Maurice, J. P., and Donovan, E. (2021). A time-dependent two-dimensional model simulation of lower ionospheric variations under intense SAID. *J. Geophys. Res.: Space Phys.*, *126*(12), e2021JA029756. https://doi.org/10.1029/2021JA029756

Liang, J., Gillies, D., Donovan, E., Parry, H., Mann, I., Connors, M., and Spanswick, E. (2022). On the green isolated proton auroras during Canada Thanksgiving geomagnetic storm. *Front. Astron. Space Sci.*, *9*, 1040092. https://doi.org/10.3389/fspas.2022.1040092

Mende, S. B., Harris, S. E., Frey, H. U., Angelopoulos, V., Russell, C. T., Donovan, E., Jackel, B., Greffen, M., and Peticolas, L. M. (2008). The THEMIS array of ground-based observatories for the study of auroral substorms. *Space Sci. Rev.*, *141*(1), 357–387. https://doi.org/10.1007/s11214-008-9380-x

Nishimura, Y., Bruus, E., Karvinen, E., Martinis, C. R., Dyer, A., Kangas, L., Rikala, H. K., Donovan, E. F., Nishitani, N., and Ruohoniemi, J. M. (2022). Interaction between proton aurora and stable auroral red arcs unveiled by citizen scientist photographs. *J. Geophys. Res.: Space Phys.*, *127*(7), e2022JA030570. https://doi.org/10.1029/2022JA030570

Partamies, N., Whiter, D., Kauristie, K., and Massetti, S. (2022). Magnetic local time (MLT) dependence of auroral peak emission height and morphology. *Ann. Geophys.*, *40*(5), 605–618. https://doi.org/10.5194/angeo-40-605-2022

Peterson, G. L. (1999). Stray light calculation methods with optical ray trace software. In *Proceedings Volume 3780, Optical Design and Analysis Software* (pp. 132–137). Denver, CO, United States: SPIE. https://doi.org/10.1117/12.363770

Picone, J. M., Hedin, A. E., Drob, D. P., and Aikin, A. C. (2002). NRLMSISE-00 empirical model of the atmosphere: Statistical comparisons and scientific issues. *J. Geophys. Res.: Space Phys.*, *107*(A12), 1468. https://doi.org/10.1029/2002JA009430

Rees, M. H., and Luckey, D. (1974). Auroral electron energy derived from ratio of spectroscopic emissions I. Model computations. *J. Geophys. Res.*, *79*(34), 5181–5186. https://doi.org/10.1029/JA079i034p05181

Sakaguchi, K., Shiokawa, K., Ieda, A., Miyoshi, Y., Otsuka, Y., Ogawa, T., Connors, M., Donovan, E. F., and Rich, F. J. (2007). Simultaneous ground and satellite observations of an isolated proton arc at subauroral latitudes. *J. Geophys. Res.: Space Phys.*, *112*(A4), A04202. https://doi.org/10.1029/2006ja012135

Seidel, F. C., Kokhanovsky, A. A., and Schaepman, M. E. (2010). Fast and simple model for atmospheric radiative transfer. *Atmos. Meas. Tech.*, *3*(4), 1129–1141. https://doi.org/10.5194/amt-3-1129-2010

Shepherd, M. G., and Shepherd, G. G. (1995). On the I(557.7 nm)I(427.8 nm) emission rate ratio in aurora. *J. Atmos. Terr. Phys.*, *57*(8), 933–943. https://doi.org/10.1016/0021-9169(94)00065-V

Shiobara, M., Spinhirne, J. D., Uchiyama, A., and Asano, S. (1996). Optical depth measurements of aerosol cloud, and water vapor using sun photometers during FIRE cirrus IFO II. *J. Appl. Meteor.*, *35*(1), 36–46. https://doi.org/10.1175/1520-0450(1996)035<0036:ODMOAC>2.0.CO;2

Solomon, S. C., Hays, P. B., and Abreu, V. J. (1988). The auroral 6300 Å emission: Observations and modeling. *J. Geophys. Res.: Space Phys.*, *93*(A9), 9867–9882. https://doi.org/10.1029/JA093iA09p09867

Solomon, S. C. (2017). Global modeling of thermospheric airglow in the far ultraviolet. *J. Geophys. Res.: Space Phys.*, *122*(7), 7834–7848. https://doi.org/10.1002/2017JA024314

Strickland, D. J., Meier, R. R., Hecht, J. H., and Christensen, A. B. (1989). Deducing composition and incident electron spectra from ground-based auroral optical measurements I: Theory and model results. *J. Geophys. Res.: Space Phys.*, *94*, 13527–13539. https://doi.org/10.1029/JA094iA10p13527

Watanabe, S., Takahashi, T., and Bennett, K. (2017). Quantitative evaluation of the accuracy and variance of individual pixels in a scientific CMOS (sCMOS) camera for computational imaging. In *Proceedings Volume 10071, Single Molecule Spectroscopy and Superresolution Imaging X* (pp. 76–83). San Francisco, California, United States: SPIE. https://doi.org/10.1117/12.2251043

Whiter, D. K., Partamies, N., Gustavsson, B., and Kauristie, K. (2023). The altitude of green OI 557.7 nm and blue N_2^+ 427.8 nm aurora. *Ann. Geophys.*, *41*(1), 1–12. https://doi.org/10.5194/angeo-41-1-2023

Zhang, Y. L., Paxton, L. J., Morrison, D., Wolven, B., Kil, H., Meng, C. I., Mende, S. B., and Immel, T. J. (2004). O/N_2 changes during 1–4 October 2002 storms: IMAGE SI-13 and TIMED/GUVI observations. *J. Geophys. Res.: Space Phys.*, *109*(A10), A10308. https://doi.org/10.1029/2004JA010441

Zhang, Y. L., Paxton, L. J., Morrison, D., Marsh, D., and Kil, H. (2014). Storm-time behaviors of O/N_2 and NO variations. *J. Atmos. Sol.-Terr. Phys.*, *114*, 42–49. https://doi.org/10.1016/j.jastp.2014.04.003